



Multiphysics modeling of particle spattering and induced defect formation mechanism in Inconel 718 laser powder bed fusion

Qian Chen¹ · Yao Fu² · Albert C. To¹

Received: 15 February 2022 / Accepted: 22 September 2022 / Published online: 4 October 2022
© The Author(s), under exclusive licence to Springer-Verlag London Ltd., part of Springer Nature 2022

Abstract

Powder particle spattering induced by the metal vapor jetting and vortex flow near the melt pool significantly influences the porosity of final product. In this work, a high-fidelity multiphysics model is developed at powder-scale that unidirectionally couples the powder spattering and laser welding simulation to study the spattering and porosity formation mechanism in laser powder bed fusion process. Vapor pressure from single-track laser welding simulation is applied as a moving boundary condition in a discrete element model to simulate particle spattering. Then, coupling simulation between the mass particles and laser welding is performed to study the interaction between melt pool and spattering particles. Two porosity formation mechanisms are observed in experiments and simulation. The first one is the spattering particles falling into melt pool directly and leaving un-melted or partially melted pores to the final product. The second mechanism is the particles near the melt track that are dragged to the melt pool bead and partially melted due to heat conduction. These partially melted particles can be observed as well in the bead region of depositions.

Keywords Laser powder bed fusion · Spattering · Multiphysics modeling · Porosity · Melt pool

1 Introduction

Laser powder bed fusion (L-PBF), one of the most popular metal additive manufacturing (AM) techniques, has gained unprecedented attention from both industry and academia owing to its capability of producing components with complex geometry and intricate internal structures. L-PBF has been widely used for automobile, aerospace, and biomedical applications to produce components that are difficult or even impossible to be fabricated by conventional manufacturing process, as well as reduce part number and simplify assembly process. However, spattering particles, particle ejected away from the hot laser spot, could oxidize during in-flight cooling, contaminate the powder bed, lead to process defects, and affect the mechanical performance of as-built part. For example, in a phenomenon called “laser

shadowing”, particle agglomerates emitted from the melt pool may partially or completely block the laser beam from powder bed, leading to shallow melt pool or leaving un-melted area inside the building part [1]. Moreover, spatter particle redeposition will change the local layer thickness of the original powder bed and lead to lack-of-fusion pores [2]. There are two types of spatters identified by high-speed camera: (1) micro-droplet spattering, also called “incandescent spatter”, caused by tearing of molten metal, and (2) cold powder particle spatter driven by the vortex flow near melt pool [3]. This incomplete melting of spatter particles brings inclusions and pores in the parts [3]. It was also reported that spatters could also increase the powder bed heterogeneity [4] and oxide inclusion [5].

Understanding better the underlying mechanism of spattering will help improve process design to stabilize the laser scanning process, decrease instabilities, and deliver parts with higher reliability. Various defect mechanisms due to spatter particles such as laser expulsion, self-replication, and laser shadowing have been revealed by the Lawrence Livermore National Laboratory (LLNL) through simulation and experiments [1]. Tang et al. [6] revealed the droplet spatter formation mechanism in the SLM process of 316L stainless steel through simulation. A viscous shear force acting on the

✉ Albert C. To
albertto@pitt.edu

¹ Department of Mechanical Engineering and Materials Science, University of Pittsburgh, Pittsburgh, PA 15261, USA

² Department of Aerospace and Ocean Engineering, Virginia Tech, Blacksburg, VA 24601, USA

keyhole wall drives the backward molten flow which forms a liquid column in the rear subsequently. The liquid column begins to neck and then is pinched off and emitted outside the melt pool as a droplet spatter. Ly et al. [7] revealed that the dominant mechanism leading to micro-droplet ejection is the vapor driven entrainment of micro-particles by ambient gas flow. Chen and Yan [8] also elaborated that vapor jetting and the consequent vortex flows are dominant in the spattering and denudation phenomena by a multiphase flow model that bi-directionally couples discrete particles and laser welding simulation. Pauzon et al. [2] studied the significant effect of using helium as the protected gas on incandescent spatter reduction.

Porosity inside the as-built part is one of the common process-induced defects which could deteriorate the mechanical performance of L-PBF part such as fatigue life. There are pore formation mechanisms that remain unclear in the L-PBF process due to the complex physics involved. Hojjatzadeh et al. [9] reported six pore formation mechanisms observed in L-PBF through high-speed camera. Zhao et al. [10] found correlation between keyhole tip instability and trapped pore in the solidification front. Process-induced pores such as lack-of-fusion pores and keyhole pores due to trapped gas have also been studied extensively [11–15]. Porosity also could come from both raw and used powder particles [16]. Hojjatzadeh et al. [17] also proposed a pore elimination approach utilizing the thermocapillary force induced by the high temperature gradient in melt region to achieve pore-free metal fabrication.

In this paper, the interaction between cold spatter particles and the melt track is studied through numerical simulations and experiments. The porosity formation mechanism associated with cold spatter particles is then revealed. The remaining content of this paper is organized as follows. In Sect. 2, the experimental details on single and multiple track depositions are presented. Section 3 presents the multiphysics modeling for laser welding process. Section 4 reports the experimental and simulation results. Section 5 gives the conclusions. The particle re-distribution simulation is presented in the Appendix.

2 Experimental details

In the printing experiment, two single tracks were deposited under the power of 285 W and scan speed of 0.96 m/s on one 80- μm -thick layer of Inconel 718 powders by the EOS M290 DMLS system. The powder size distribution is summarized in Table 1. The distance between two single tracks is set to be 0.25 mm, 0.50 mm, 0.75 mm, and 1.0 mm in the building process. All the single tracks were scanned by the EOS M290 DMLS system using an Ytterbium fiber laser with a maximum power of 400 W, a wavelength of 1060–1100 nm

Table 1 The distribution of IN718 powder particles used from the vendor

Particle diameter (μm)	Percentage (%)
5	5.00
10	5.00
20	6.35
30	7.96
36	13.63
43	18.28
51	19.20
61	15.97
73	7.58
80	1.05

and focus diameter of 100 μm . The focal length is 410 mm. Spattering particles from the first deposited single track can also influence the second track. Therefore, more spattering particles are expected when depositing the second track which increases the chance of interaction between the melt track and falling particles. All the as-built specimens were cross-sectioned in the middle by electrical discharge machine along the plane perpendicular to the laser scanning direction. The samples were mounted and grounded to 1200 grit, followed by vibrator polishing, then etched in a solution of 15 parts acetic acid, 10 parts nitric acid, and 10 parts hydrochloric.

3 Multiphysics models

In this work, three different models are developed and coupled to simulate spattering phenomenon during L-PBF process and study the porosity formation mechanisms. The workflow of the proposed modeling work is presented in Fig. 1. In step 1, the powder spreading process is simulated by Flow-3D DEM module to generate the powder bed with a mean layer thickness of 80 μm . The size distribution of powder particles from the vendor in Table 1 is used in this simulation. In step 2, a moving pressure boundary condition is applied along the center line of the powder bed to induce spattering. In step 3, a model that couples laser welding and falling solid spattering particles is developed by Flow-3D welding module.

3.1 Laser welding model calibration

To calibrate the simulation setup including absorptivity, evaporation model and boundary conditions, the melt pool cross sections from simulation for single-track deposition on powder bed with a layer thickness of 80 μm and triple-track deposition in S-pattern on powder bed with a layer

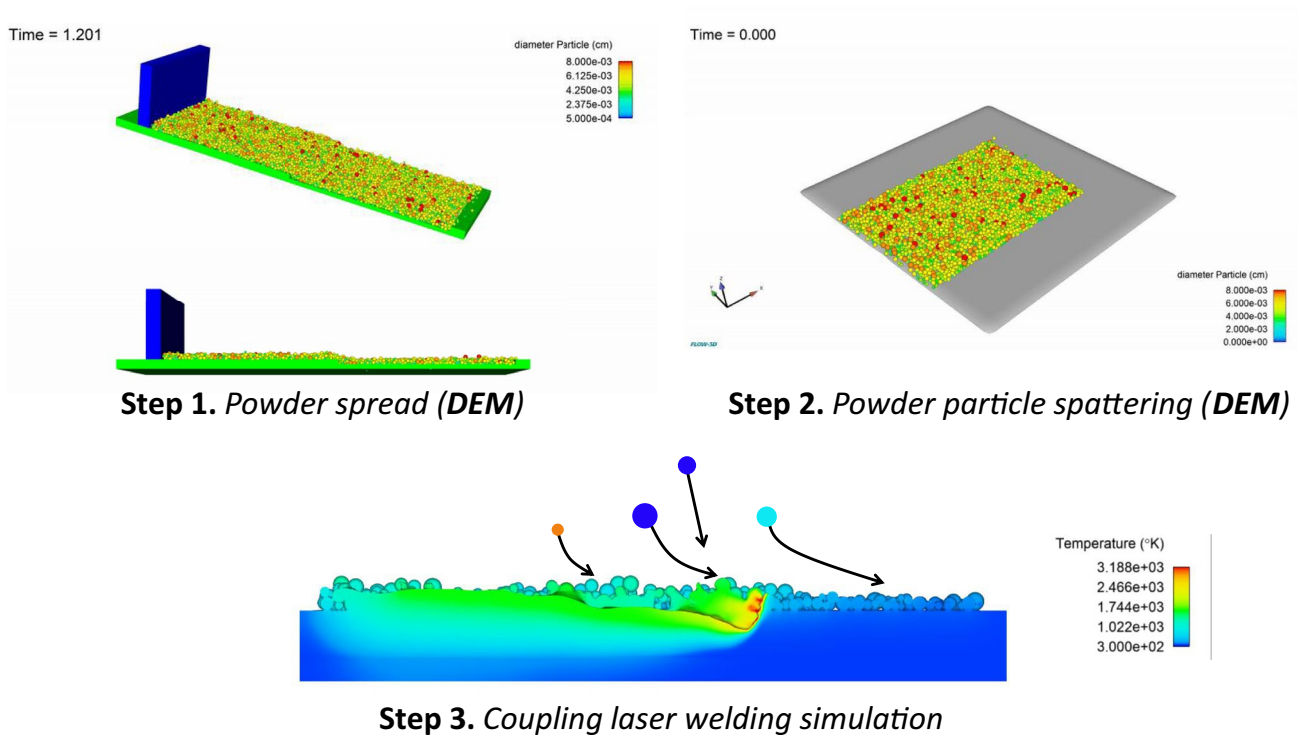


Fig. 1 Flowchart of the proposed spattering modeling

thickness of 40 μm are compared to experimental ex situ measurements.

The comparison of melt pool cross section for single-track deposition between simulation and experiment is presented in Fig. 2. In the experiment, we spread a layer of powder with a layer thickness of 80 μm . It can be found that melt pool bead height is around 80 μm in both simulation and experiment. The melt pool width in simulation is 8.28% larger than experiment, while the melt pool width is 8.37% smaller than experiment. The difference of melt pool dimensions between simulation and experiment is attributed to the variation of powder bed layer thickness. In ex situ cross section, two sphere particles are found to have attached to

the melt pool bead on the right and left side, respectively. This is caused by the particle entrapment due to molten flow during the laser scanning process.

Calibration for the triple-track deposition simulation is performed as well. The comparison of melt pool cross section between simulation and experiment is presented in Fig. 3. It can be found that the melt pool depth increases from the first track to the third track (from left to right) in both simulation and ex situ measurement, which is attributed to the residual heat. The absorptivity value is set to 0.28, and the simulation is performed on a bare plate without powder particles. In the experiment, we spread a layer of powder with a layer thickness of 40 μm . However, the purging took half an hour, and most

Fig. 2 Melt pool cross section comparison between simulation and experiment for single track

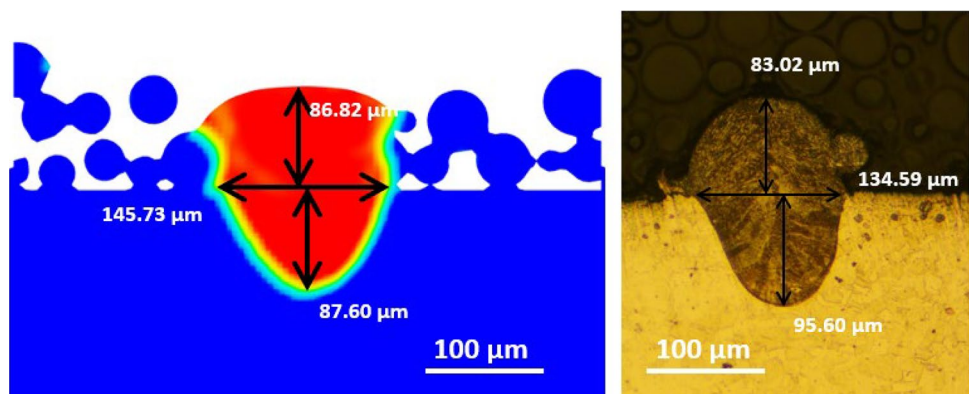
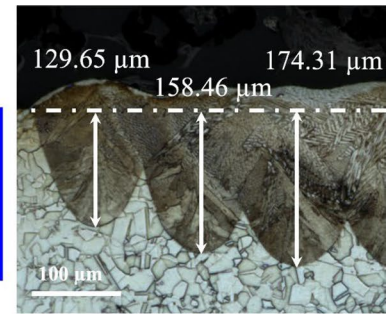
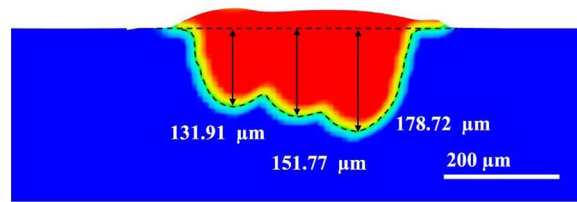


Fig. 3 Melt pool cross section comparison between simulation and experiment for triple tracks



the spread particles were blown away. It can be found that the melt pool depths have a good agreement with experimental measurements. The top region of the melt pools in simulation is similar to the experiment measurement as well.

3.2 Laser welding model coupled with mass particles

A coupling simulation is developed to study the interaction between spattering particles and laser welding track and reveal the pore formation mechanism associated with the entrainment of mass particles into unsolidified melt pool. Three particle sources are added into the single-track laser welding simulation. The mass particles with initial velocity coming out of each particle source are shown in Fig. 4. The laser power is 285 W, scan speed is 1.0 m/s, and the powder bed before spattering is used.

The molten metal flow is taken as Newtonian and incompressible in the simulation. Mass continuity, momentum, and energy conservations in Eqs. (1)–(3) are solved:

$$\nabla \cdot \vec{v} = 0 \tag{1}$$

$$\frac{\partial \vec{v}}{\partial t} + (\vec{v} \cdot \nabla) \vec{v} = -\frac{1}{\rho} \nabla P + \mu \nabla^2 \vec{v} + \vec{g} [1 - \alpha(T - T_m)] \tag{2}$$

$$\frac{\partial h}{\partial t} + (\vec{v} \cdot \nabla) h = \frac{1}{\rho} (\nabla \cdot k \nabla T) \tag{3}$$

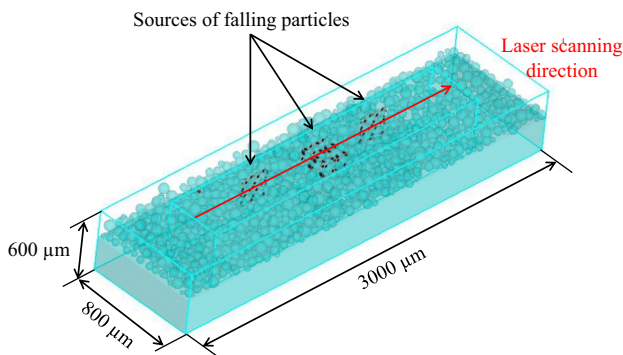


Fig. 4 Setup for simulation model that couples DEM and laser welding

where \vec{v} is the velocity vector, \vec{p} is the pressure, μ is the viscosity, \vec{g} is the gravity vector, α is the thermal expansion coefficient, ρ is the density, h is the specific enthalpy, and k is the thermal conductivity.

The location of melt pool free surface is tracked by the volume of fluid (VOF) method, in which the volume fraction of fluid occupying each mesh in the computation domain is defined by the fluid fraction F :

$$\frac{\partial F}{\partial t} + \nabla \cdot (F \vec{v}) = 0 \tag{4}$$

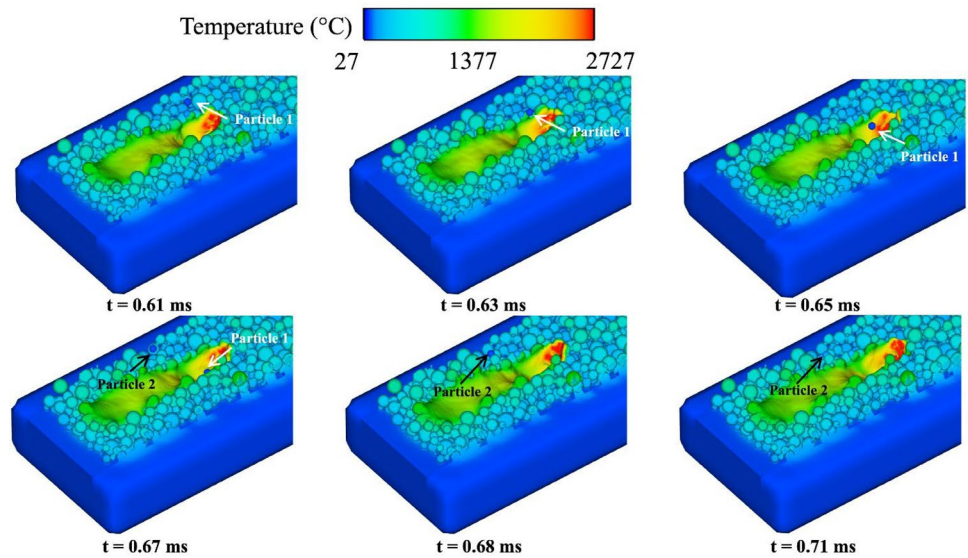
where $0 \leq F \leq 1$. For a reasonable and precise description of the L-PBF process, the physical model is customized based on the process conditions and accounts for buoyant flow, Marangoni convection, vapor recoil pressure, and heat radiation in the simulation. The thermal properties of the IN718 alloy and the coefficients used in the simulation can be found in Ref. [18].

4 Results and discussion

A coupling simulation is developed to study the interaction between spattering particles and laser welding track and reveal the pore formation mechanism associated with the entrainment of mass particles into unsolidified melt pool. Three particle sources are added into the single-track laser welding simulation. The laser power is 285 W, scan speed is 1.0 m/s, and the powder bed before spattering is used. Snapshots of interaction between falling particles and laser welding are presented in Fig. 10. It can be observed that the particles falling into the melt pool are melted due to the heat transfer between molten flow and particles, while particles falling on the powder bed near melt track are heated up but not melted.

Figure 5 shows the snapshots of the simulation coupling laser welding and falling mass particles. At 0.61 ms, the first falling particle right above the melt track (as indicated by the white arrow) has a temperature 80 °C. At 0.63–0.67 ms, this particle enters into the depression zone caused by vapor evaporation pressure. This particle is then melted by the

Fig. 5 Snapshots of coupling simulation between mass particles and laser welding



molten flow and cannot be tracked anymore at 0.68 ms. At 0.67 ms, there is another particle falling on the powder bed near the laser melt track as indicated by the black arrow. At 0.68 ms, this particle contacts with a few particles on the powder bed. Due to the heat conduction between falling particle and powder bed, the particle temperature rises to around 300 °C at 0.71 ms.

The cross section where the falling mass particles are attached to the melt region is shown in Fig. 6. Mass particles falling on the powder bed near the melt track are heated up. In the real building process, these falling particles will change the local powder bed morphology, and large particles can also lead to lack of fusion in the neighboring track or subsequent layers. These particles attached to melt pool bead

are not completely melted and increase the porosity of the as-built part. Moreover, these particles also serve as origin of pores in the subsequent layers.

Attachment of powder particles to melt pool is also observed in the ex situ melt pool cross section measurement as shown in Fig. 7. These melt pools in Fig. 7 all have one particle with different diameter attached to the melt pool bead surface. The left melt pool has a very small attachment which is caused by the falling small particles while the middle melt pool has a larger particle that connects the neighboring powder bed and melt pool bead and leaves a void. The right melt pool has a particle in circular shape which may not be completely melted by laser scanning in neighboring tracks or subsequent layers.

Fig. 6 Cross section where mass particles attached to melt region

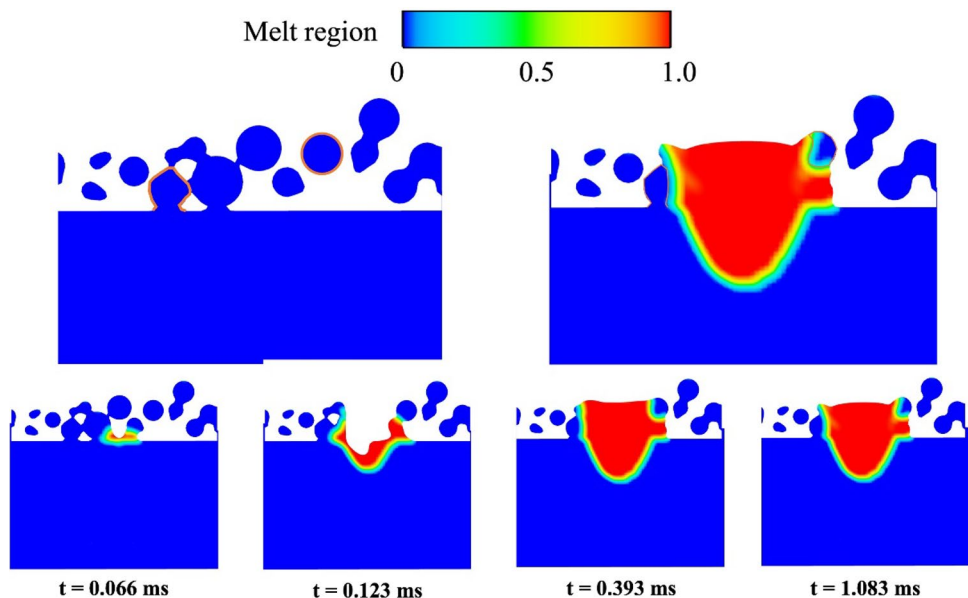
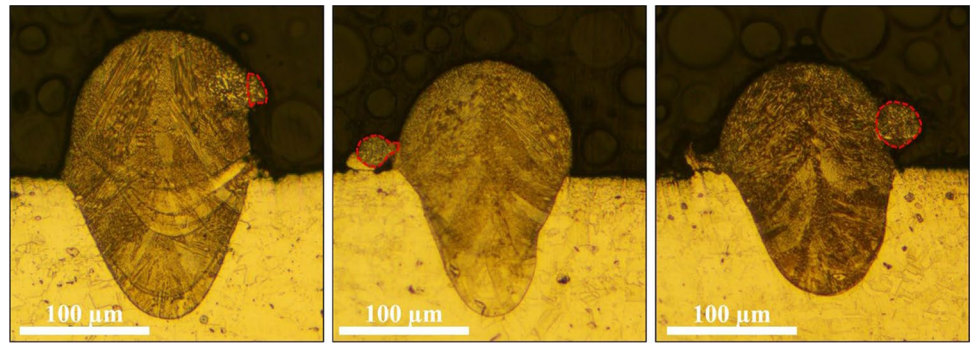


Fig. 7 Cross section where mass particles attached to melt region

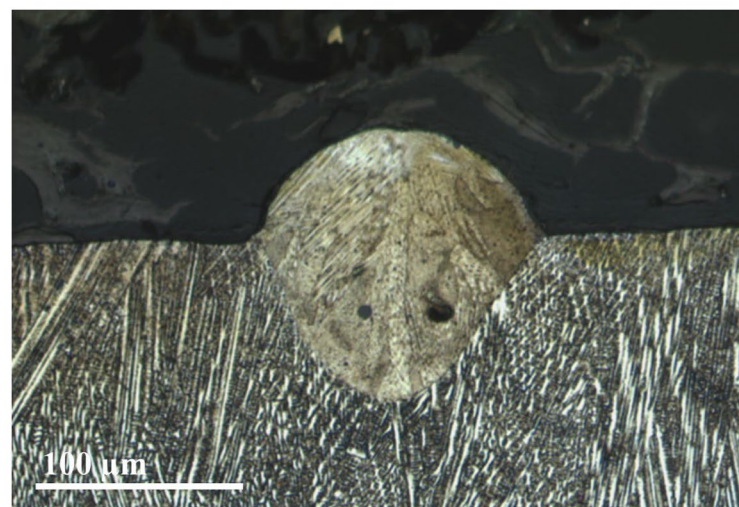
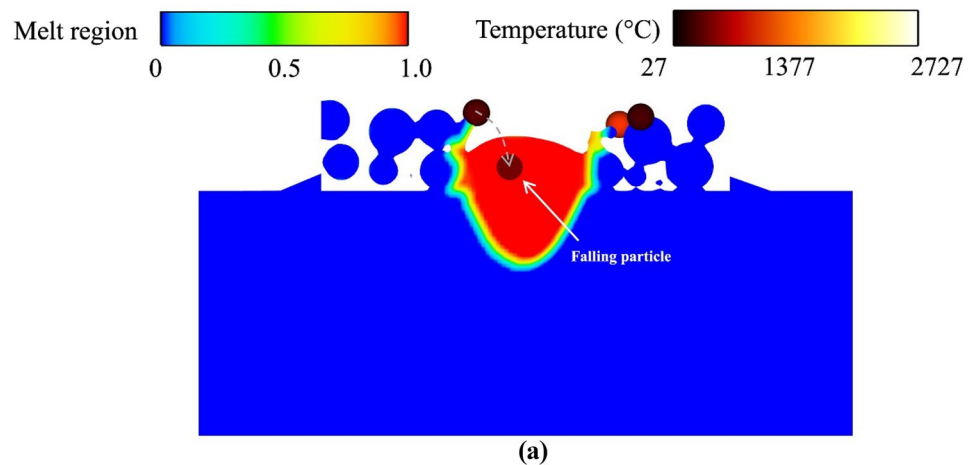


The coupling between falling mass particles and melt pool is presented in Fig. 8a. The moving laser melts the powder bed and forms a melt pool first. Then, particles with a falling speed of ~ 10 m/s enters into the molten pool. Some particles are in contact with the melt pool surface and then are ejected away due to the pressure inside the melt pool. There are also some particles fall into the melt pool and then are melted by the molten flow due to heat transfer. Among these particles, some of the large particles cannot be

completely melted by the molten pool, and a pore may be formed due to this partial melting after melt pool solidification. These particles which are ejected away from the melt pool have a speed around ~ 10 m/s and will fall elsewhere on the powder bed and leads to local layer thickness variation. In the cross-section measurement, unmelted particles inside the melt pool are also observed as shown in Fig. 8b.

Compared to the experimental measurement on single track deposition under the same laser power and scan speed on bare

Fig. 8 Cross section where mass particles attached to melt region. **a** Simulation result; **b** experiment result



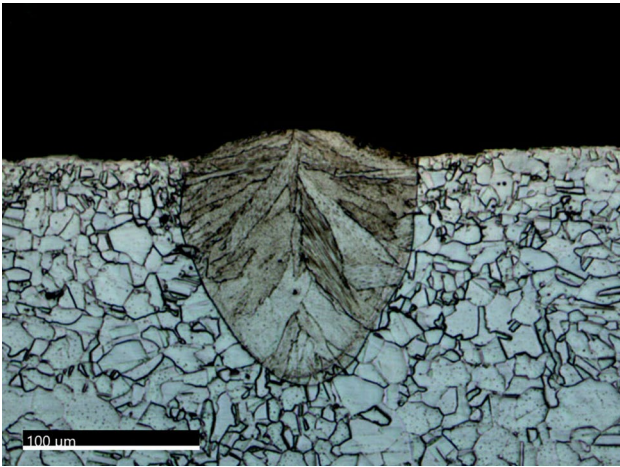


Fig. 9 Cross section of melt pool on bare plate without powder particles

plate without any particles as shown in Fig. 9. In contrast to the two large pores inside the melt pool as shown in Fig. 8b, the melt pool deposited on the bare plate under the same laser power and scan speed does not have any pores inside. This is a circumstantial evidence to the proposed porosity formation mechanisms that ejected particles fall into the melt pool and are not fully melted.

Figure 10 shows a schematic of melt pool arrangement in two consecutive layers in the L-PBF process to illustrate the likelihood of pore formation due to the above spattering mechanism. Note that there is a shift of $55\ \mu\text{m}$ (half of the hatch spacing) along horizontal direction between these two layers. Suppose that once the first layer deposition is done, there are three melt pools and two pores formed. The pore attached to melt pool bead is indicated by the orange dot while the pore due to falling solid particle entrainment is indicated by the black dot. The pore attached on melt pool bead will be completely removed during the second layer deposition. The blue melt pool on the left side will fully cover this pore, implying that it will likely be melted and eliminated. However, the

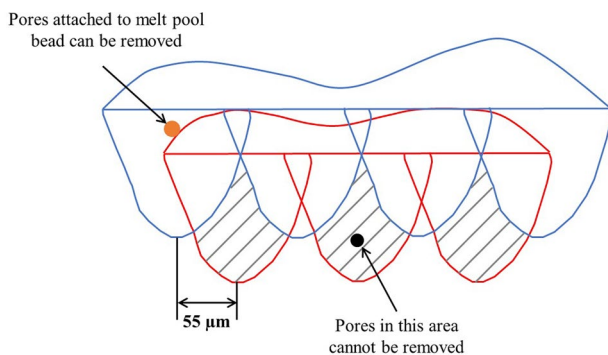


Fig. 10 Schematic of melt pool overlaps within two layers and pore elimination

pore near the melt pool bottom due to solid particle entrainment cannot be re-melted. When depositing the second layer, these melt pools in the middle are not able to re-melt this pore because of the spatial location. This pore will be left inside the part as a permanent defect and may lead to degraded fatigue performance.

5 Conclusion

In this paper, a modeling approach that couples the mass particle with laser welding process is proposed to study the interaction between spatter particles and melt track and the defect formation mechanism associated with spattering. Multiphysics models were developed and calibrated by ex situ cross-sectional measurements. The major conclusions are presented as follows:

- A unidirectional coupling model was developed by Flow-3D DEM to simulate the powder particle movement during the deposition process. A moving pressure boundary condition was applied along the melt track to represent the recoil pressure that blows away the neighboring solid particles;
- Laser welding model that considers the falling spatter particle was developed by Flow-3D to study the interaction between solid spatter particle and the melt track. It was found that depending on the location, these falling particles could be completely melted, partially melted or re-deposited on the neighboring powder bed.
- Powder particle attachment to melt pool bead is observed in both simulation and single-track deposition experiment. Particles near the melt track may not be completely melted during the deposition process. It was revealed that pores caused by particle attachment can be eliminated by the subsequent layer building;
- Another pore formation mechanism is the solid particle falls into the melt pool and cannot be completely melted by the molten flow. This pore usually cannot be eliminated by the subsequent layer printing since it locates near the bottom of melt pool.

Appendix

The model for spattering particle re-distribution is developed by the Flow-3D discrete element method (DEM) module. A moving velocity boundary condition is applied to the bottom of power bed along the laser scan track. An upward vertical speed of $150\ \text{m/s}$ is applied to model the moving vapor jet that blows up the particle near the melt track and leads to denudation. This moving velocity boundary condition is a poor man's approach to model the complicated particle ejection and denudation which are caused by the complex

interaction between powder particles, metal vapor jet and gas flow near the melt pool. To accurately modeling this phenomenon requires multiphysics models which consider the heat and mass transfer and fluid dynamics inside the melt pool. The scope of this paper is to study the interaction between melt pool and particles falling down which are previously blown up by the vapor jet. This spattering particle re-distribution model aims at finding the speed of falling particles with different size. Therefore, we developed this poor-man's approach to get the speed for the next step laser welding simulation while saving the computation cost. The unidirectional DEM coupling model, as shown in Fig. 11, is briefly discussed as follows:

- A moving jet hole with a radius of 80 μm is in the middle of the substrate underneath the powder bed generated by powder settling and spreading simulation.
- The moving speed of the jet hole equals to the laser scan speed of 1 m/s.
- The boundary condition for the moving jet hole is a velocity boundary condition and the vertical speed is set as 150 m/s corresponding to the vapor coming out the depression zone.

Spherical powder particles are used in the DEM model. The governing equations for the translational and rotational motions of individual powder particles are:

$$m_i \frac{d^2 \mathbf{r}_i}{dt^2} = m_i \mathbf{g} + \sum_j (\mathbf{F}_{n,ij} + \mathbf{F}_{t,ij} + \mathbf{F}_{c,ij}) \quad (5)$$

$$I_i \frac{d^2 \boldsymbol{\theta}_i}{dt^2} = \sum_j \mathbf{T}_{ij} = \sum_j \mathbf{R}_i \times \mathbf{F}_{t,ij} \quad (6)$$

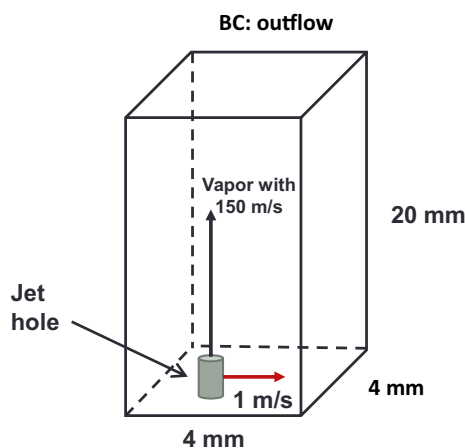


Fig. 11 Schematic of spattering model developed by discrete element method

where m_i is the mass of the powder particle, \mathbf{r}_i is the position vector, $\boldsymbol{\theta}_i$ is the angular displacement, \mathbf{R}_i is the radius of particle. I_i is the moment of inertia, $\mathbf{F}_{n,ij}$ and $\mathbf{F}_{t,ij}$ are the contact force along normal and tangential direction. $\mathbf{F}_{c,ij}$ is the cohesion force. \mathbf{T}_{ij} is the moment caused by particle j . Hertz-Mindlin contact model [19] is employed to compute the contact force $\mathbf{F}_{n,ij}$ and $\mathbf{F}_{t,ij}$, while JKR cohesion model [20] is used to compute the cohesion force $\mathbf{F}_{c,ij}$. More details can be found in [21].

In the simulation, the powder bed generated by powder settling and spreading before spattering simulation has a mean layer thickness of 80 μm and is densely packed with a packing density of 53%. The powder particles after the jet hole moving along the center line of the powder bed with a scan speed of 1.0 m/s and flow speed of 150 m/s become scattered and the powder bed becomes spread out. There are a large number of particles coming back to the denudation zone with a transverse (along y direction) or vertical (along z direction) speed which indicates a potential pore formation mechanism due to these particles.

Acknowledgements The financial support from the Department of Energy under Award number DE-FE0031774 is gratefully acknowledged. Technical support from Flow Science is acknowledged.

Author contribution Qian Chen: conceptualization, investigation, methodology, experiment, simulation, writing – original draft, and writing – review and editing. Yao Fu: experiment, writing – original draft. Albert. C. To: conceptualization, investigation, methodology, writing – original draft, and writing – review and editing.

Funding This study was supported by the financial support from the Department of Energy Award Number DE-NE0008994.

Availability of data and material Not applicable.

Code availability Not applicable.

Declarations

Ethics approval Not applicable.

Consent to participate The consent to submit this paper has been received explicitly from all co-authors.

Conflict of interest The authors declare no competing interests.

References

1. Khairallah SA, Martin AA, Lee JR, Guss G, Calta NP, Hammons JA, Nielsen MH, Chaput K, Schwalbach E, Shah MN (2020) Controlling interdependent meso-nanosecond dynamics and defect generation in metal 3D printing. *Science* 368(6491):660–665
2. Pazon C, Hoppe B, Pichler T, Dubiez-Le Goff S, Forêt P, Nguyen T, Hryha E (2021) Reduction of incandescent spatter with helium

- addition to the process gas during laser powder bed fusion of Ti-6Al-4V. *CIRP J Manuf Sci Technol* 35:371–378
3. Liu Y, Yang Y, Mai S, Wang D, Song C (2015) Investigation into spatter behavior during selective laser melting of AISI 316L stainless steel powder. *Mater Des* 87:797–806
 4. Anwar A, Pham QC (2018) Study of the spatter distribution on the powder bed during selective laser melting. *Addit Manuf* 22:86–97
 5. Pazon C, Raza A, Hryha E, Forêt P (2021) Oxygen balance during laser powder bed fusion of Alloy 718. *Mater Des* 201:109511
 6. Tang P, Xie H, Wang S, Ding X, Zhang Q, Ma H, Yang J, Fan S, Long M, Chen D (2019) Numerical analysis of molten pool behavior and spatter formation with evaporation during selective laser melting of 316L stainless steel. *Metall Mater Trans B* 50(5):2273–2283
 7. Ly S, Rubenchik AM, Khairallah SA, Guss G, Matthews MJ (2017) Metal vapor micro-jet controls material redistribution in laser powder bed fusion additive manufacturing. *Sci Rep* 7(1):1–12
 8. Chen H, Yan W (2020) Spattering and denudation in laser powder bed fusion process: multiphase flow modelling. *Acta Mater* 196:154–167
 9. Hojjatzadeh SMH, Parab ND, Guo Q, Qu M, Xiong L, Zhao C, Escano LI, Fezzaa K, Everhart W, Sun T (2020) Direct observation of pore formation mechanisms during LPBF additive manufacturing process and high energy density laser welding. *Int J Mach Tools Manuf* 153:103555
 10. Zhao C, Parab ND, Li X, Fezzaa K, Tan W, Rollett AD, Sun T (2020) Critical instability at moving keyhole tip generates porosity in laser melting. *Science* 370(6520):1080–1086
 11. Teng C, Pal D, Gong H, Zeng K, Briggs K, Patil N, Stucker B (2017) A review of defect modeling in laser material processing. *Addit Manuf*
 12. Khairallah SA, Anderson AT, Rubenchik A, King WE (2016) Laser powder-bed fusion additive manufacturing: physics of complex melt flow and formation mechanisms of pores, spatter, and denudation zones. *Acta Mater* 108:36–45
 13. Bayat M, Mohanty S, Hattel JH (2019) Multiphysics modelling of lack-of-fusion voids formation and evolution in IN718 made by multi-track/multi-layer L-PBF. *Int J Heat Mass Transf* 139:95–114
 14. Tang M, Pistorius PC, Beuth JL (2017) Prediction of lack-of-fusion porosity for powder bed fusion. *Addit Manuf* 14:39–48
 15. Gong H, Rafi K, Gu H, Starr T, Stucker B (2014) Analysis of defect generation in Ti-6Al-4V parts made using powder bed fusion additive manufacturing processes. *Addit Manuf* 1:87–98
 16. Clayton J (2014) Optimising metal powders for additive manufacturing. *Met Powder Rep* 69(5):14–17
 17. Hojjatzadeh SMH, Parab ND, Yan W, Guo Q, Xiong L, Zhao C, Qu M, Escano LI, Xiao X, Fezzaa K (2019) Pore elimination mechanisms during 3D printing of metals. *Nat Commun* 10(1):3088
 18. Chen Q, Zhao Y, Strayer S, Zhao Y, Aoyagi K, Koizumi Y, Chiba A, Xiong W, To AC (2021) Elucidating the effect of preheating temperature on melt pool morphology variation in Inconel 718 laser powder bed fusion via simulation and experiment. *Addit Manuf* 37:101642
 19. Di Renzo A, Di Maio FP (2004) Comparison of contact-force models for the simulation of collisions in DEM-based granular flow codes. *Chem Eng Sci* 59(3):525–541
 20. Johnson K, Greenwood J (1997) An adhesion map for the contact of elastic spheres. *J Colloid Interface Sci* 192(2):326–333
 21. Chen H, Wei Q, Zhang Y, Chen F, Shi Y, Yan W (2019) Powder-spreading mechanisms in powder-bed-based additive manufacturing: experiments and computational modeling. *Acta Mater* 179:158–171

Publisher's Note Springer Nature remains neutral with regard to jurisdictional claims in published maps and institutional affiliations.

Springer Nature or its licensor holds exclusive rights to this article under a publishing agreement with the author(s) or other rightsholder(s); author self-archiving of the accepted manuscript version of this article is solely governed by the terms of such publishing agreement and applicable law.